Research Article **Open Access**

Alessia Allevi*, Silvia Cassina, and Maria Bondani

Super-thermal light for imaging applications

https://doi.org/10.1515/qmetro-2017-0004
Received July 28, 2017; accepted November 20, 2017

Abstract: We report on a new classical light source useful for ghost-imaging applications. The light is obtained by frequency doubling a conventional speckle pattern having an overall multi-mode thermal distribution. The frequency-doubled light acquires a super-thermal distribution, which induces higher correlations at a beam splitter and, as a consequence, a higher visibility in ghost-imaging protocols.

Keywords: Photon statistics; Nonlinear optics; Photodetectors; Imaging

1 Introduction

The term "ghost imaging" is commonly used to indicate several different imaging techniques that share the use of two spatially correlated beams to reconstruct the image [1, 2]. In the general scheme of ghost imaging, one of the beams illuminates an object, and the light it transmits or reflects is collected by a single detector called "bucket" detector. At the same time, the other beam is measured by a spatial-resolving detector which does not interact with the object. The image of the object is recovered by correlating the intensities measured by the bucket detector with the intensities measured by each pixel of the spatial-resolving detector [3]. The geometry of light propagation required to reconstruct the image depends on the specific kind of correlated beams in use: ghost imaging protocols with twin beams require the use of lenses [4–7], while those performed with thermal light can be lensless [8, 9].

***Corresponding Author: Alessia Allevi:** Dipartimento di Scienza e Alta Tecnologia, Università degli Studi dell'Insubria, and Istituto di Fotonica e Nanotecnologie, Consiglio Nazionale delle Ricerche, via Valleggio 11, I-22100 Como, Italy, E-mail: alessia.allevi@uninsubria.it
Silvia Cassina: Dipartimento di Scienza e Alta Tecnologia, Università degli Studi dell'Insubria, via Valleggio 11, I-22100 Como, Italy, E-mail: s.cassina@studenti.uninsubria.it
Maria Bondani: Istituto di Fotonica e Nanotecnologie, Consiglio Nazionale delle Ricerche, via Valleggio 11, I-22100 Como, Italy, E-mail: maria.bondani@uninsubria.it

As an alternative to ghost imaging employing physically separated beams, computational ghost imaging techniques have also been proposed [10, 11]. In this case, thermal light is generated with a spatial light modulator and only the bucket detector is used beyond the object. The correlation to recover the ghost image is then evaluated between the output of the bucket detector and the computed pattern imposed by the spatial light modulator. Hence computational ghost imaging highly simplifies the experimental setup.

The quality of the reconstructed ghost image, quantified for instance in terms of visibility, depends on the value of the intensity correlations between the beams [12]. As an example, ghost images obtained with twin beams are expected to have higher visibility than those obtained with thermal light divided at a beam splitter, even if the experimental non-ideality of twin beams can make this difference negligible [7, 8]. For a light beam divided at a beam splitter, the amount of correlations depends on the statistical properties of the light itself [13]. In fact, it is well known that the cross-correlation function between the beams exiting a beam splitter is linked to the autocorrelation function of the light entering the beam splitter, so that highly super-Poissonian light generates high intensity correlations.

Recently, we have demonstrated that the second harmonic field generated from thermal light is endowed with a super-thermal distribution, that is its variance is larger than that of a single-mode thermal field at the same intensity. As a consequence, super-thermal light produces higher correlations than thermal light [14].

In this paper, we exploit the potential of super-thermal light to obtain higher-visibility ghost images in a single-beam ghost-imaging scheme, where the object is artificially selected on the sensor of a CCD camera and the correlations are calculated between the integrated intensity values corresponding to the object and each pixel of the entire image.

The paper is organised as follows: In Section 2 we review the statistical properties of super-thermal light produced by second-harmonic generation. Such properties are experimentally verified in the mesoscopic regime with photon-number-resolving detectors (Section 3). In Section 4 a speckle pattern having super-thermal statistics is

used to produce ghost images of different objects and the results are compared with the same images obtained with thermal light. Finally, in Section 5 we draw some conclusions.

2 Super-thermal statistics

It is well-known [15] that the photon-number distribution of a multi-mode thermal field, in which the μ modes are assumed to be equally populated, is given by

$$P_{\rm th}(n) = \frac{(n+\mu-1)!}{n!(\mu-1)!(\langle n\rangle/\mu+1)^{\mu}(\mu/\langle n\rangle+1)^{n}}, \qquad (1)$$

where $\langle n\rangle$ is the mean value of the distribution. The variance of the statistics in Eq. (1) reads as $\sigma^2_{\rm th}(n) = \langle n\rangle(\langle n\rangle/\mu + 1)$ and its Fano factor is given by

$$F_{\rm th}(n) = \frac{\sigma_n^2}{\langle n\rangle} = \frac{\langle n\rangle}{\mu} + 1. \qquad (2)$$

Since the quantity on the right side of Eq. (2) is larger than 1, the multi-mode thermal statistics is called superPoissonian, being $F = 1$ the value of Fano factor for Poissonian statistics. Equation (1) describes the statistical distribution of the number of photons for multi-mode thermal states as they would be detected by a perfect detector. In general, since real detectors reveal light with a non-unit detection efficiency, the statistics of detected photons could be different from that of photons. However, if the detection process is described by the Bernoullian distribution

$$B(n,m) = \binom{n}{m}\eta^m(1-\eta)^{n-m}, \qquad (3)$$

the functional form of Eq. (1) remains the same upon the substitution $\langle n\rangle \to \eta\langle n\rangle \equiv \langle m\rangle$. Hence, the statistics of detected photons is again multi-mode thermal. Recently, we have shown that when the second-harmonic generation process is applied to the multi-mode thermal field described by Eq. (1) the second-harmonic field is characterised by a different statistics [14]. In particular, by using a classical approach it is possible to demonstrate that the photon-number distribution for detected photons is given by

$$P_{\rm sth}(m) = \frac{\Gamma[1/2+m+\mu/2]\Gamma[m+\mu/2]}{4\sqrt{\pi}m!(\mu-1)!\{\langle m\rangle/[\mu(1+\mu)]\}^{(\mu+1)/2}} \times U\left[\frac{1}{2}+m+\frac{\mu}{2},\frac{3}{2},\frac{\mu(\mu+1)}{4\langle m\rangle}\right], \qquad (4)$$

in which $\langle m\rangle$ is the mean number of detected photons, μ is the number of modes in the fundamental beam, $\Gamma[j]$ is the Gamma function, and $U[i,j,k]$ is the Tricomi confluent hypergeometric function. Hereafter, we will call the statistics in Eq. (4) super-thermal statistics. We note that the variance of the photon-number distribution in Eq. (4), $\sigma^2_{\rm sth}(m) = 2(2\mu+3)/[\mu(\mu+1)]\langle m\rangle^2 + \langle m\rangle$, is definitely larger than that of a multi-mode thermal field having the same mean photon number and the same number of modes. The corresponding Fano factor reads as

$$F_{\rm sth}(m) = \frac{2(2\mu+3)}{\mu(\mu+1)}\langle m\rangle + 1 = \frac{1}{\zeta}\langle m\rangle + 1, \qquad (5)$$

in which we defined $\zeta = \mu(\mu+1)/[2(2\mu+3)]$. Note that the expressions for the variance of multi-mode thermal and super-thermal lights are the same provided the substitution $\mu \to \zeta < \mu$, that is by considering a sort of multi-mode thermal light with less modes. By comparing Eqs. (2) and (5) it is quite evident that, given a fixed number of modes, the super-thermal statistics is characterised by more fluctuations than the multi-mode thermal one, especially for low numbers of μ.
Indeed, if μ is large, it is really hard to distinguish the two distributions.

An alternative approach to investigate the statistical properties of quantum states of light is to evaluate the Glauber second-order auto-correlation function [16]

$$g^{(2)}(n) = \frac{\langle :n^2:\rangle}{\langle n\rangle^2} = \frac{\langle n^2\rangle}{\langle n\rangle^2} - \frac{1}{\langle n\rangle} = 1 + \frac{F(n)-1}{\langle n\rangle}, \qquad (6)$$

where $:\cdot:$ indicates the normal ordering operation. In particular, by inserting the expression of the Fano factor of the multi-mode thermal statistics (see Eq. (2)) in Eq. (6), we obtain:

$$g^{(2)}_{\rm th}(n) = 1 + \frac{1}{\mu}. \qquad (7)$$

To evaluate the analog expression for super-thermal light, we notice that the relation between the Fano factor of photons is linked to that of detected photons through

$$F(n) = \frac{F(m)-1+\eta}{\eta}, \qquad (8)$$

By substituting Eq. (5) in Eq. (8), it can be easily demonstrated that the expressions of $F_{\rm sth}(m)$ and $F_{\rm sth}(n)$ coincide upon the substitution $\langle m\rangle \to \langle n\rangle$. Hence, by inserting the expression of the Fano factor of the super-thermal statistics in Eq. (6) we get:

$$g^{(2)}_{\rm sth}(n) = 1 + \frac{1}{\zeta}. \qquad (9)$$

Note that the $g^{(2)}(n)$ function is not invariant under Bernoullian detection. However, it can be easily demonstrated [17] that the analogous expression of $g^{(2)}$ for detected photons is linked to that of photons as follows

$$g^{(2)}(m) = g^{(2)}(n) + \frac{1}{\langle m\rangle} = 1 + \frac{F(m)-1}{\langle m\rangle} + \frac{1}{\langle m\rangle}, \qquad (10)$$

in which $\langle m \rangle$ is the mean number of detected photons and $g^{(2)}(m) = \langle m^2 \rangle / \langle m \rangle^2$. For large values of detected photons the term $1/\langle m \rangle$ on the right side of Eq. (10) can be neglected and the expressions of $g^{(2)}(m)$ and $g^{(2)}(n)$ coincide.

All the quantities described so far can be equivalently used to characterise the statistical properties of an optical state. However, there are situations in which the values of F and $g^{(2)}$ are not sensitive enough to distinguish between similar states. An example is given by the super-thermal states with a large number of modes [14]. In this case, a possible alternative measurement is given by the calculation of the photon-number correlations between the two outputs of a beam splitter at which the light under study has been divided. Indicating the two outputs as c and d, the correlation coefficient can be defined as [13]:

$$\gamma(m) = \frac{\langle (m_c - \langle m_c \rangle)(m_d - \langle m_d \rangle) \rangle}{\sqrt{\sigma^2(m_c)\sigma^2(m_d)}}. \tag{11}$$

For the multi-mode thermal field described by Eq. (1), the expression of γ reads as:

$$\gamma_{\rm th}(m) = \frac{\sqrt{\langle m_c \rangle \langle m_d \rangle}}{\sqrt{(\langle m_c \rangle + \mu_c)(\langle m_d \rangle + \mu_d)}}, \tag{12}$$

whereas for the super-thermal field described by Eq. (4), the correlation coefficient γ is given by

$$\gamma_{\rm sth}(m) = \frac{\sqrt{\langle m_c \rangle \langle m_d \rangle}}{\sqrt{(\langle m_c \rangle + \zeta_c)(\langle m_d \rangle + \zeta_d)}}. \tag{13}$$

Note that, as expected, $\gamma_{\rm sth}(m) > \gamma_{\rm th}(m)$.

3 Experimental results: statistical properties

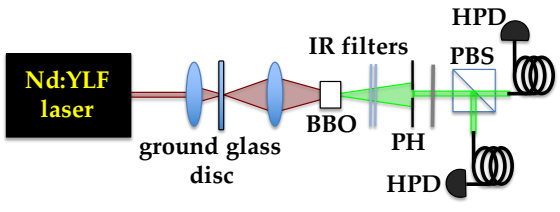

Figure 1: (Colour online) Sketch of the experimental setup used for the generation and characterisation of the statistical properties of super-thermal light. BBO, β-barium-borate crystal; PBS, polarizing cube beam splitter; PH, pin-hole; HPD, hybrid photodetector.

In order to produce an optical state characterised by the photon-number distribution in Eq. (4), we focused the fundamental beam (at 1047 nm) emitted by a Nd:YLF laser regeneratively amplified at 500 Hz on the surface of a rotating ground-glass disc to generate a pseudo-thermal field (see Fig. 1) exhibiting the typical speckle pattern. At a distance of 100 cm from the disc, a portion of the infrared light was mildly focused into a β-barium-borate (BBO) crystal (cut-angle = 22.8 deg, 4-mm-long) and frequency doubled at 523 nm. After the removal of the residual infrared light by means of some coloured glass filters, a portion of the generated green light having a size roughly corresponding to a single speckle was selected by means of a 150-µm-wide pin-hole (PH) and then divided at a polarizing cube beam splitter (PBS) preceded by a half-wave plate for the fine control of the balancing between the two arms. At the two PBS outputs, two multi-mode fibers (core diameter = 600 μm) collected the light and delivered it to two commercial photon-number resolving (PNR) detectors. In more detail, we used a pair of hybrid photodetectors (HPD, mod. RU10467U-40, Hamamatsu Photonics), which are detectors composed of a photocathode followed by an avalanche diode operated below breakdown threshold. Their outputs were amplified, synchronously integrated and digitised. In order to investigate the statistical properties of the detected light, sequences of 100,000 single shots were collected for different intensity values of the fundamental beam. To this aim, a variable neutral density filter was placed in front of the BBO crystal.

By following the self-consistent method already described in Refs. [18, 19], the outputs of the detection chain, expressed in terms of voltages, were converted into numbers of detected photons. In Fig. 2 we show the reconstruction of two detected-photon-number distributions having different mean values. For a direct comparison, the experimental data, shown as grey columns + error bars, are superimposed to the theoretical expectations described by Eq. (1) (black dots) and Eq. (4) (red dots), where we used the experimental mean numbers of photons and left μ as the only fitting parameter. In particular, we notice that in the case of multi-mode thermal statistics we got a number of modes lower than 1, which is actually meaningless from the physical point of view, whereas in the case of super-thermal statistics we roughly obtained 1 mode, as expected. The different agreement between the data and each one of the theoretical curves is stressed by the vertical logarithmic scale. In particular, we notice that increasing the number of photons, the multi-mode thermal distribution does not fit the data any more, whereas the super-thermal one perfectly matches them. In order to quantify the closeness between the experimental data and each theoretical expectation we evaluated the fidelity, defined as $f = \sum_m \sqrt{P_{\rm exp}(m) P_{\rm theor}(m)}$, where $P_{\rm exp}(m)$ ($P_{\rm theor}(m)$)

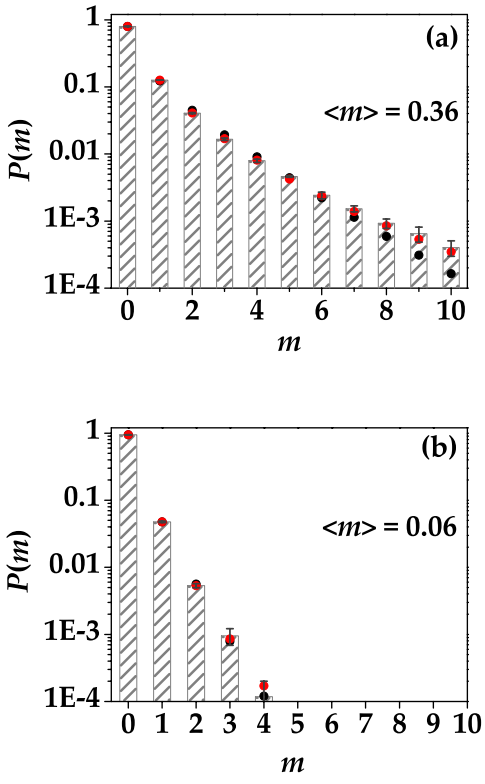

Figure 2: (Colour online) Reconstruction of the distributions of detected photons for $\langle m \rangle = 0.36$ (panel (a)) and $\langle m \rangle = 0.06$ (panel (b)). Grey columns + error bars: experimental data; black dots: multi-mode thermal fit; red dots: super-thermal fit. The corresponding values of the fidelity are $f_{\mathrm{th}} = 99.964 \pm 0.077\%$ and $f_{\mathrm{sth}} = 99.991 \pm 0.075\%$ in panel (a) and $f_{\mathrm{th}} = 99.998 \pm 0.102\%$ and $f_{\mathrm{sth}} = 99.999 \pm 0.102\%$ in panel (b), respectively.

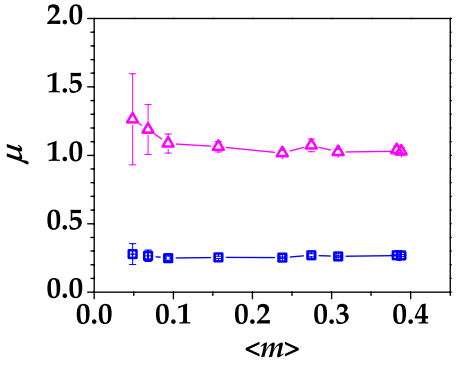

Figure 3: (Colour online) Number of modes obtained from the fitting curves as a function of the mean number of photons measured at one PBS output. Magenta empty triangles + line: numbers of modes obtained as fitting parameters for the super-thermal curve; blue empty squares + line: numbers of modes obtained as fitting parameters for the multi-mode thermal curve.

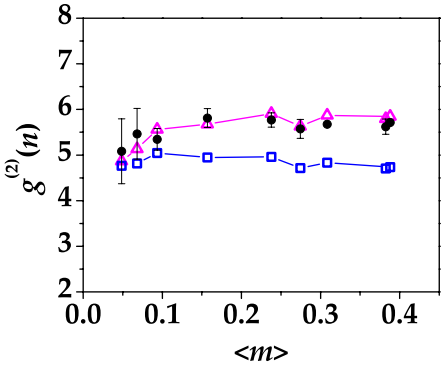

Figure 4: (Colour online) $g^{(2)}(n)$ autocorrelation function for photons as a function of the mean number of photons detected at one PBS output. Black dots: experimental data; magenta empty triangles + line: theoretical expectation in the case of super-thermal statistics; blue empty squares + line: theoretical expectation in the case of multi-mode thermal statistics.

is the experimental (theoretical) distribution and the sum extends up to the maximum number of detected photons above which the statistics become negligible. As reported in the caption of the figure, the experimental distributions are closer to the super-thermal statistics. As a further confirmation of the fact that the light selected by the pinhole exhibits a photon-number distribution according to Eq. (4), in Fig. 3 we present the number of modes obtained as fitting parameters for the sequence of data taken at one PBS output. The blue empty squares + line (the line is used to guide the eye) correspond to the number of modes in the case of the multi-mode thermal fitting curve, whereas the magenta empty triangles + line (the line is used to guide the eye) were obtained in the case of the super-thermal fitting curve. As already mentioned, the multi-mode fit yields a number of modes lower than 1, a meaningless result for the model. On the contrary, the values obtained from the super-thermal distribution are very close to 1, attesting the correct selection of a single coherence area at 523 nm.

As anticipated in Section 2, an alternative description of the statistical properties of light can be obtained by evaluating the Glauber autocorrelation function.

Since the detection chain we employed gives us access to the number of detected photons, we evaluate the $g^{(2)}(m)$ for detected photons in order to obtain $g^{(2)}(n)$ through Eq. (10).

In Fig. 4 we present the autocorrelation function $g^{(2)}(n)$ for the sequence of data taken at one PBS output at different mean values. The experimental data (black dots) are shown together with the theoretical expectations calculated according to Eq. (7) for the multi-mode thermal model (blue empty squares + line) and to Eq. (9) for the

super-thermal one (magenta empty triangles + line), in which we used the numbers of modes obtained by the fitting curves.

To better emphasise how the super-thermal model is more appropriate to describe the data than the multi-mode thermal one, in Fig. 5 we plot the experimental correlation coefficient γ as a function of the mean number of photons at the PBS outputs. In the same figure we present the two different theoretical expectations. Note that the better superposition of data to the super-thermal expectation can be also quantified by calculating the reduced chi-square. In fact, for the super-thermal model we obtained $\chi^2 = 1.06$, whereas for the multi-mode thermal one we obtained a definitely worse value, that is $\chi^2 = 14.16$.

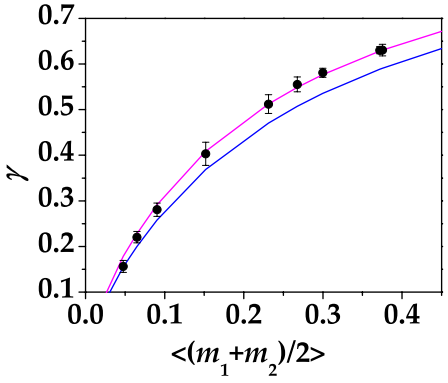

Figure 5: (Colour online) Correlation coefficient γ between the two PBS outputs. Black dots: experimental data; magenta line: theoretical expectation according to super-thermal model; blue line: theoretical expectation according to multi-mode thermal model.

4 Experimental results: application to imaging

The high intensity fluctuations that characterise the super-thermal light make it interesting for imaging applications. The experiment we realised is just a proof-of-principle, but the results we achieved are really promising for a real ghost-image implementation.

In order to investigate the parameters to be taken into account, like the value of the $g^{(2)}$ autocorrelation function and the visibility, we used the same kind of scheme adopted in Refs. [10, 11]. At variance with the traditional ghost-imaging technique already presented in the Introduction, in the scheme proposed by Shapiro the spatial-resolving detector is replaced with a "virtual detector" obtained by calculating the propagation of the field not interacting with the object. The image is then reconstructed

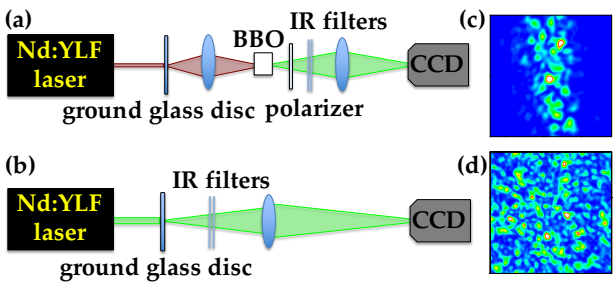

Figure 6: (Colour online) Left panels: Sketch of the experimental setups for the application of super-thermal light (in panel (a)) and thermal light (in panel (b)) to imaging. BBO, β-barium-borate crystal; CCD, camera. Right panels: Typical single-shot images of the speckle pattern exhibited by super-thermal light (panel (c)) and by thermal light (panel (d)).

by correlating the calculated field patterns with the intensities measured by the bucket detector in the object arm. In this imaging configuration only one light beam and one photodetector are required, and this choice indicates that "ghost-image formation is intrinsically due to classical coherence propagation". Following this proposal, in our scheme we used only one beam that we detected by means of a CCD camera, which is a spatial-resolving detector. Since a detector of this kind can be as well operated as a bucket detector by integrating the intensity coming from different pixels, the ghost image was obtained by simply correlating the same light as collected by the bucket detector and as detected by a spatial-resolving one. From the technical point of view, this experimental scheme allows the optimisation of the results as it avoids possible beam distortion introduced by the optical elements. To the same aim, as the objects we decided to use only numerical masks applied in post processing to the sequence of data. By following the same approach already used in [20], the objects were obtained by multiplying the recorded single-shot speckle patterns by 1 in the mask region and by 0 outside. It is worth noting that the employed scheme makes a fair comparison possible between the results obtained both with the super-thermal light and with the thermal one. The two experimental schemes we realised are shown in Fig. 6, in which panel (a) refers to super-thermal light, and panel (b) to thermal one. In both cases the light was at the same wavelength (523 nm). According to panel (a), the infrared light emitted by the laser already mentioned in Section 3 was sent to a rotating ground-glass disc in order to generate thermal light. At nearly 100 cm from

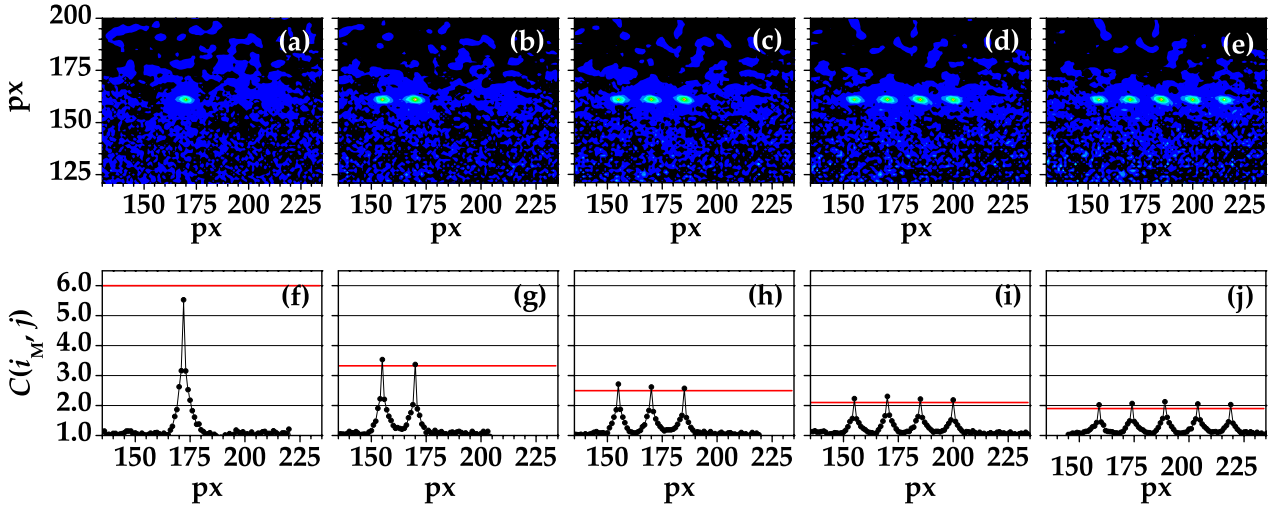

Figure 7: (Colour online) Upper panels: Correlation images C reconstructing the 5 different objects illuminated by super-thermal light. Lower panels: Corresponding vertical sections $C(i_M, j)$, where i_M is the horizontal coordinate of the maximum. The red lines indicate the theoretical expected values.

the disc, a portion of this light was sent by a 15-cm-focal-length lens to the same BBO crystal described above. Note that the nonlinear medium is in the Rayleigh range of the lens. Upon the removal of the infrared light by means of a polarizer and some coloured glass filters, the second-harmonic field at 523 nm, naturally diverging from the nonlinear crystal, was sent to the sensor of a CCD camera (mod. DCU223M, Thorlabs, 1024 × 768 pixels, 4.65-µm pixel size).

For what concerns the scheme in panel (b), the second harmonic of the Nd:YLF laser was directly extracted from the source and sent to the same ground-glass disc shown in panel (a). Some coloured glass filters were used to remove possible residual of infrared light coming from the laser source and superimposed to the green light. Moreover, a 15-cm-focal-length lens was used to send a portion of pseudo-thermal light to the CCD camera in such a way that the typical speckle size is roughly the same in both schemes (see the contour plots in Fig. 6(c) and (d) for a direct comparison). Note also that in both cases we can consider the speckles as monochromatic. This means that the modes involved in the illumination of the objects and in the reconstruction of the images are only spatial modes. By comparing panels (c) and (d), we note that the light converted to green by the second-harmonic process is limited in the horizontal plane by the phase-matching condition, which reduces the size of the possible objects to be imaged. Phase matching also introduces a modulation on the generated light that prevents the imaging of objects extended in the horizontal direction.

For each kind of light, we acquired a sequence of $K = 6600$ consecutive single-shot images while the disc was rotating. All the images were subtracted by the dark, obtained with the camera sensor closed, and then a 2×2 binning procedure was applied to each frame in order to avoid the autocorrelation of the single pixel in the data processing.

In order to control the number of modes involved in the imaging process, for the objects we chose an increasing number of vertically aligned points, each one having the same size as the CCD pixel size and corresponding to a single speckle and thus to a single mode. All the points have been chosen in such a way that the speckles to which they belong are well separated from each other. In particular, we considered objects composed of 1, 2, 3, 4, and 5 points. Note that this choice can be also seen as a simple way to transmit a binary code, in which the chosen points correspond to the logic bit 1, while the absence of points represents the logic bit 0. Coding more points allows the transmission of more information in parallel.

Given that k is the index of each single-shot image and by assuming that the indices p identify the speckles illuminating the object, whose total number is P, the correlated images were obtained by correlating the sum of the intensities of the pixels composing the object, $I_k^{\text{obj}} = \sum_{p=1}^{P} I_{kp}^{\text{obj}}$, and each of the pixels of coordinates (i, j) contained in the same image, and then averaging over all the images in the

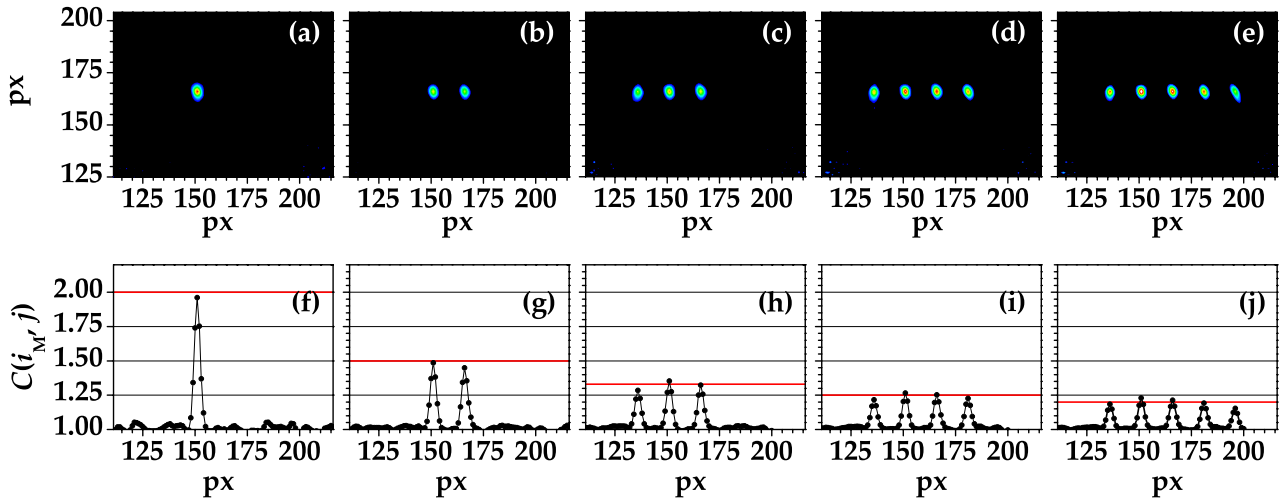

Figure 8: (Colour online) Upper panels: Correlation images C reconstructing the 5 different objects illuminated by thermal light. Lower panels: Corresponding vertical sections $C(i_M, j)$, where i_M is the horizontal coordinate of the maximum. The red lines indicate the theoretical expected values.

sequence [20, 21]:

$$C(i,j) = \frac{1}{K}\sum_{k=1}^{K} I_k^{\mathrm{obj}} I_k^{(\mathrm{i,j})}. \tag{14}$$

In Fig. 7 we present the results obtained by exploiting the super-thermal light. In the upper panels we show the portions of the correlation images reconstructing the objects, and in the lower panels the corresponding vertical sections, from which it is possible to extract information about the maximum values of C achieved in each case. In Fig. 8 we show the results obtained with thermal light. In particular, we note that for each object the maximum value of $g^{(2)}$ achieved with thermal light is always lower than the corresponding one obtained with super-thermal light. This result reflects the relation between the value of the autocorrelation function and the number of modes, already shown in Eqs. (7) and (9). In more detail, we notice that since the CCD camera is a macroscopic detector, the two expressions of $g^{(2)}$ simplify as the last term on the right side can be neglected. For the same reason, the expression for detected photons formally coincides with that for photons (see Eq. (10)).

For a more direct comparison, in Fig. 9(a) we show the maximum value of C, C_M, as a function of the number of modes for the two kinds of light states under investigation. The experimental data are shown as dots, whose error bars were obtained by dividing the collected images into three subsequences of 2200 images, whereas the theoretical predictions are presented as empty circles + line and were cal-

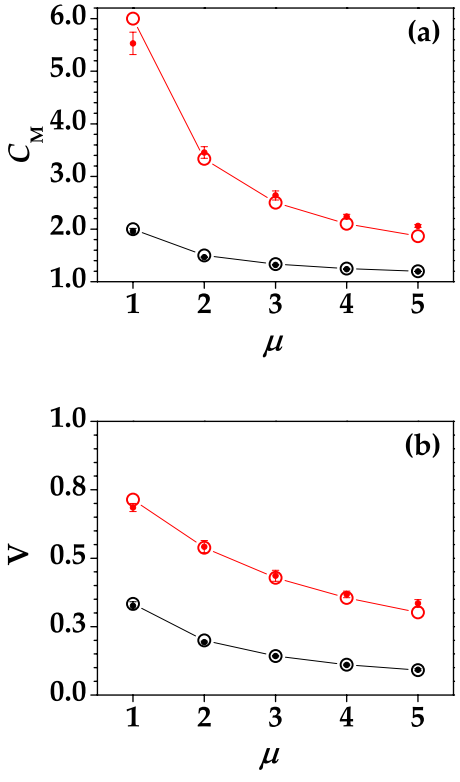

Figure 9: (Colour online) (a): Maximum value C_M of the correlation image as a function of the number of modes. (b) Visibility as a function of the number of modes. Black (red) dots: experimental data obtained by illuminating the objects with thermal (super-thermal) light. Open circles + line: theoretical expectation.

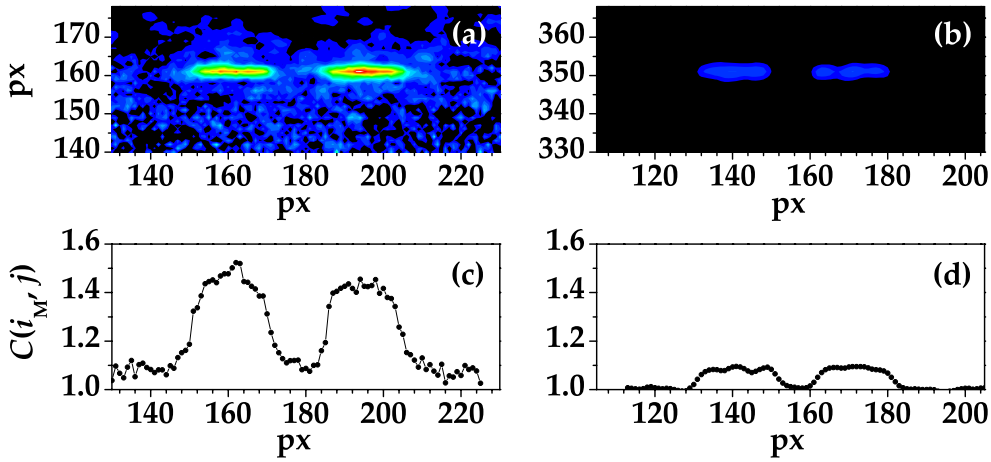

Figure 10: (Colour online) Upper panels: Correlation images C reconstructing the 2-lines object illuminated by super-thermal (panel (a)) and by thermal (panel (b)) light. For a more direct comparison the intensity scale is the same in the two contour plots. Lower panels: Corresponding vertical sections $C(i_M, j)$, where i_M is the horizontal coordinate of the maximum.

culated according to Eqs. (7) and (9) by setting the number of points in the object as the number of modes.

To better stress the difference between the results achieved with super-thermal and thermal light, we also consider the visibility of the images, which is a typical parameter for imaging. Formally, this quantity is defined as [12]

$$V = \frac{g^{(2)}_{\mathrm{IN}} - g^{(2)}_{\mathrm{OUT}}}{g^{(2)}_{\mathrm{IN}} + g^{(2)}_{\mathrm{OUT}}}, \tag{15}$$

in which $g^{(2)}_{\mathrm{IN}}$ is the value of the autocorrelation function inside the image and $g^{(2)}_{\mathrm{OUT}}$ the value of the background. In the case of thermal light, the expression in Eq. (15) reduces to $V_{\mathrm{th}} = 1/(1 + 2\mu)$, whereas in the case of super-thermal light it is given $V_{\mathrm{sth}} = 1/(1 + 2\zeta)$. For each choice of μ, $V_{\mathrm{sth}} > V_{\mathrm{th}}$, thus encouraging the use of super-thermal light instead of a pseudo-thermal one to improve the visibility of the reconstructed images. As both the visibilities approach 0 for $\mu \to \infty$, this limits the maximum number of bits transmitted in parallel. However, note that given a fixed value of acceptable experimental visibility for the implementation of the protocol, the maximum number of bits that can be transmitted is definitely larger for super-thermal light than for thermal light.

In Fig. 9(b), we show V as a function of the number of modes μ for the data presented in Figs. 7 and 8. The experimental data are shown as dots, whereas the theoretical predictions are presented as empty circles + line.

In order to prove the goodness of the super-thermal light for imaging applications in a more realistic scenario, we also considered a more extended numerical object made by two consecutive slits, each one 20 pixels long. The experimental results are shown in Fig. 10 for the two cases: Panels (a), and (c) refer to super-thermal light, while panels (b) and (d) to thermal light. In the upper panels we show the correlation images and in the lower panels the vertical sections. In particular, from panels (c) and (d) we can conclude that the maximum value of C achieved with super-thermal light is definitely higher than the corresponding one achieved with thermal light.

5 Discussion and Conclusions

In conclusion, we have demonstrated that super-thermal light obtained by the process of second-harmonic generation applied to a multi-mode thermal field is endowed with statistical properties that make it appealing for imaging applications. In particular, we have shown that, compared to thermal states, this kind of optical state displays higher intensity fluctuations, which lead to the observation of higher photon-number correlations. The investigation of the statistical properties has been performed in the mesoscopic intensity domain by means of a pair of HPD detectors. Indeed, by applying the self-consistent method of analysis to the outputs of the detectors, we were able not only to reconstruct the photon-number distribution of detected photons, but also to calculate the autocorrelation function and the shot-by-shot photon-number correlations between the two outputs of a balanced beam splitter at which super-thermal light was divided. For all the

quantities that we considered, the experimental data are in excellent agreement with the theoretical model. Thanks to the existence of a higher level of photon-number correlations, we were able to implement a proof-of-principle experiment in which super-thermal light was used, in competition with thermal light, for the illumination of some one-dimensional objects and the reconstruction of the corresponding ghost images. We have shown that the visibility of the images is higher in the case of super-thermal light than in the case of thermal light.

The main drawbacks of the use of super-thermal light generated by second harmonics come from the properties of phase matching. The region of converted light is limited to a quite narrow vertical strip in which the intensity distribution is not homogeneous. This limits the choice of possible objects to vertical ones. Nevertheless, this condition can be enough for the transmission of binary codes in parallel.

Acknowledgement: We thank Alessandro Tucci Bronzuoli for his help in the laboratory.

References

[1] M. D'Angelo and Y. H. Shih, Laser Phys. Lett. **2,** 567 (2005).
[2] A. Gatti, E. Brambilla, and L. A. Lugiato, Prog. Opt. **51,** 251 (2008).
[3] D. Klyshko, Photons and Nonlinear Optics (Gordon and Breach, New York, 1988).
[4] P. H. Souto Ribeiro, S. Padua, J. C. Machado da Silva, and G. A. Barbosa, Phys. Rev. A **49,** 4176 (1994).
[5] D. V. Strekalov, A. V. Sergienko, D. N. Klyshko, and Y. H. Shih, Phys. Rev. Lett. **74,** 3600 (1995).
[6] T. B. Pittman, Y. H. Shih, D. V. Strekalov, and A. V. Sergienko, Phys. Rev. A **52,** R3429 (1995).
[7] M. Bondani, A. Allevi, and A. Andreoni, Eur. Phys. J. Special Topics **203,** 151 (2012).
[8] F. Ferri, D. Magatti, A. Gatti, M. Bache, E. Brambilla, and L. A. Lugiato, Phys. Rev. Lett. **94,** 183602 (2005).
[9] D. Zhang, Y. H. Zhai, L. A. Wu, and X. H. Chen, Opt.Lett. **30,** 2354 (2005).
[10] J. H. Shapiro, Phys. Rev. A **78,** 061802(R) (2008).
[11] Y. Bromberg, O. Katz, and Y. Silberberg, Phys. Rev. A **79,** 053840 (2009).
[12] A. Gatti, M. Bache, D. Magatti, E. Brambilla, F. Ferri and L. A. Lugiato, J. Mod. Opt. **53,** 739 (2006).
[13] A. Allevi, M. Bondani, and A. Andreoni, Opt. Lett. **35,** 1707 (2010).
[14] A. Allevi and M. Bondani, Opt. Lett. **40,** 3089 (2015).
[15] L. Mandel and E. Wolf, Optical coherence and quantum optics (Cambridge University Press, Cambridge, 1995).
[16] R. J. Glauber, Quantum Optics and Electronics (Gordon and Breach, New York, 1965).
[17] A. Allevi and M. Bondani, Antibunching-like behavior of mesoscopic light, to appear in Sci. Rep. (2017).
[18] M. Bondani, A. Allevi, A. Agliati, and A. Andreoni, J. Mod. Opt. **56,** 226 (2009).
[19] A. Andreoni and M. Bondani, Phys. Rev. A **80,** 013819 (2009).
[20] T. Iskhakov, A. Allevi, D. A. Kalashnikov, V. G. Sala, M. Takeuchi, M. Bondani, and M. Chekhova, Eur. Phys. J. Special Topics **199,** 127 (2011).
[21] A. Allevi and M. Bondani, J. Opt. **19,** 064001 (2017).